# Non-linear elastic properties of plasma-sprayed zirconia coatings and associated relationships with processing conditions

Y. Liu [a], T. Nakamura [a,*], V. Srinivasan [b], A. Vaidya [b,1], A. Gouldstone [b], S. Sampath [b]

[a] Center for Thermal Spray Research, Department of Mechanical Engineering, State University of New York at Stony Brook, NY 11794, USA
[b] Center for Thermal Spray Research, Department of Materials Science and Engineering, State University of New York at Stony Brook, NY 11794, USA

## Abstract

Low-temperature thermal cycling of plasma-sprayed zirconia coatings via curvature measurements revealed their in-plane non-linear behavior. This feature arises from the unique layered, porous and cracked morphology of thermal-sprayed ceramic materials. The non-linear aspect can be quantified by a novel data interpretation procedure consisting of modified beam bending analysis and inverse analysis. This versatile procedure requires minimum measurement preparation and computational effort, and its non-linear model enables correct data interpretations otherwise not possible with the previous assumption of linear elastic models. Using this procedure, various specimens were tested to investigate the effects of processing conditions. Results are interpreted in the context of microstructural changes in the plasma-sprayed coatings due to differences in particle state upon impact and coating build-up. The implications of this study are significant for the thermo-mechanical design of strain-tolerant ceramic coatings in thermal barrier applications.
© 2007 Acta Materialia Inc. Published by Elsevier Ltd. All rights reserved.

Keywords: Plasma-sprayed coatings; Ceramic coatings; Curvature measurement; Non-linear stress–strain relation; Inverse analysis

## 1. Introduction

Thermal spray (TS) is a well-established processing technology for the fabrication of thick coatings of ceramics and metals on a variety of substrates. These coatings are used extensively as protective layers against wear, high temperature and other harsh conditions. TS ceramic coatings are produced through successive impingement of molten droplets on a prepared substrate, resulting in a lamellar microstructure with pores and cracks. Accordingly, coating mechanical properties are highly dependent on the defect architecture of the coating and thus strongly related to the complex deposition processes and related processing conditions [1–11]. For instance, in the case of ceramics, the feedstock powder and the processing conditions of particles all affect the nature of the deposit formation dynamics and the ensuing properties of coatings.

Although it is well understood that desired or application-specific microstructures can, to a first approximation, be obtained by varying feedstock powder and processing parameters, a quantitative description in terms of properties has yet to be satisfactorily achieved. Kroupa and co-workers [12,13] built physical models relating theoretical defect geometries to macroscopic non-linear mechanical response. The non-linear behavior of ceramic coatings was also observed in other tests. Harok and Neufuss [14] reported such behavior of atmospheric plasma-sprayed (APS) $ZrSiO_4$ in four-point bend tests and noted that the mechanical behavior is elastic because ceramics generally do not exhibit plasticity at room temperature. A similar phenomenon is found by Eldridge et al. [15] that plasma-sprayed yttria stabilized zirconia (YSZ) coatings exhibit non-linear elastic behavior, and the modulus increases with applied stress because of coating compaction. Another bend test combined with strain analysis reported increasing

in-plane stiffness of YSZ coatings with compressive stress but decreasing stiffness under larger tensile stress [16]. Though a number of studies have elucidated the non-linear behavior of thermally sprayed ceramic coatings, the relation of such reasoning to process variation or, put simply, a robust method of comparison of different TS coatings, needs to be developed. This paper uses a technique to extract non-linear elastic coating properties by inverse analysis of substrate curvature measurements during thermal cycling. Then, it presents the results of such analyses on a range of plasma-sprayed (PS) YSZ coatings, obtained from a number of different processing conditions, and interprets them in the context of defect architecture. This work has important implications for both coating design and performance reliability.

## 2. Substrate curvature measurements

### 2.1. Background

Measurement of substrate curvature during thermal cycling is a well-established method for extracting the mechanical properties of thin films and thick and/or graded coatings [17–21]. Briefly, the bilayer film–substrate system is subjected to a temperature excursion $\Delta T$ that imposes thermal mismatch strain in the film. The resulting film stress depends on the constitutive properties, and the unbalanced force (stress integrated through film thickness) causes substrate curvature $\Delta\kappa$. For sufficiently thin films and coatings, it may be shown that stress in the film is uniform through-thickness, and the general expression for beam bending due to intrinsic film stress may be simplified to the Stoney formula [22]. For thicker specimens (as is the case here), the curvature solutions must be obtained with an alternate method. If both coating and substrate are linear elastic, the curvature change during spraying and cooling can be expressed as [23]

$$\Delta\kappa = \frac{6E_s E_c ht(h+t)\Delta\alpha\Delta T}{E_s^2 h^4 + E_c^2 t^4 + 2E_s E_c ht(2h^2 + 3ht + 2t^2)} \quad (1)$$

Here, $t$ and $h$ are the thickness of film/coating and substrate, respectively, and $E_s$ and $E_c$ are the elastic modulus of the substrate and coating, respectively. $\Delta\alpha$ is the difference in thermal expansion coefficients of substrate $\alpha_s$ and film/coating $\alpha_c$, and $\Delta T$ is the temperature change. The above equation with measured $\Delta\kappa - \Delta T$ record is used to determine the coating modulus $E_c$ (via the quadratic formula). Further complications arise if the coating has non-linear elastic properties: a different formulation is necessary to determine the unknown properties, as described in Section 3.

### 2.2. Experimental procedure

Fig. 1a shows a schematic of the substrate curvature test, and salient points are described here (details in [24]).
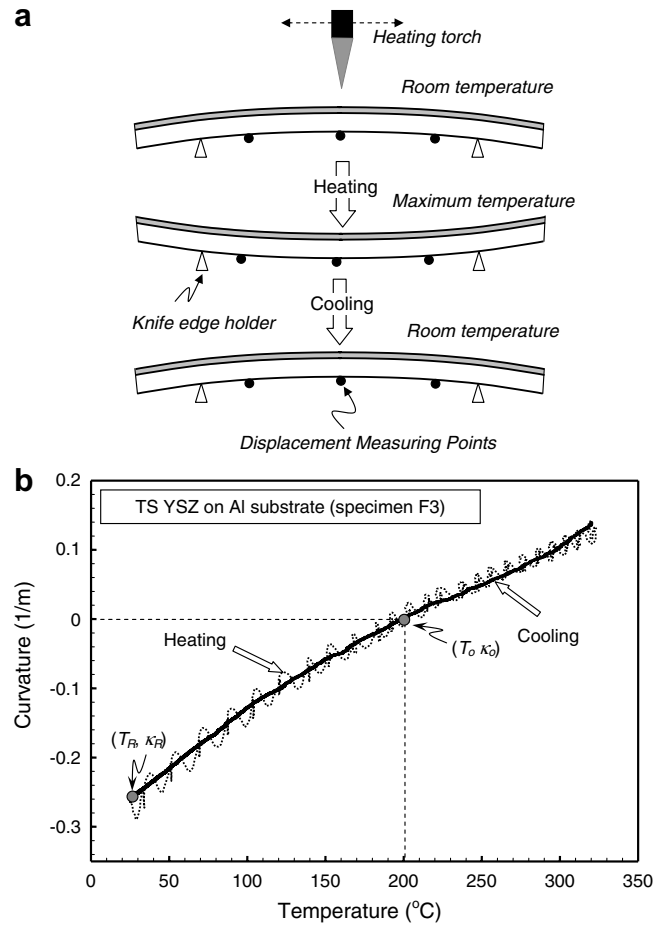


Fig. 1. (a) Schematic of curvature change as coating and substrate is thermal cycled by a moving torch along the coating surface. (b) Measured curvature during thermal cycle of YSZ coating on Al substrate. The heating curvature is shown by dashed lines, while the cooling curvature is shown by a dark solid curve. Here, $T_0$ denotes the temperature when the curvature is zero $\kappa_0$. Also, $\kappa_R$ is the room temperature curvature.

The method uses non-contact laser-based displacement sensing on the back of a substrate, with a resolution of a few microns; multiple laser displacement sensors allow for precise extraction of the radius of curvature. In addition, the temperature of the substrate is also monitored through multi-point temperature sensing using thermocouples attached to the substrate. Typical in-plane dimensions of the specimens are $230 \times 25.4$ mm. The thickness of the coating varies (via experimental design), $t = 250$–800 μm, while that of the substrate is $\sim h = 3$ mm. The original device was used to examine curvature changes during spraying and post-spray cool down to extract the residual stresses and elastic modulus of metallic and ceramic coatings. However, the YSZ coating post-deposition continues to exhibit transient microcracking phenomena and, as such, the cooling curve from deposition was unsuitable for non-linear data extraction. To achieve this, the coating–substrate system is further heated by passing a hand torch (usually MAPP gas) multiple times over the coating and is left to cool under forced air convection. Typically,

it takes 2 min to heat up and ~7 min to cool down. There are large fluctuations in curvature measurements while the specimen is heated, produced by the movement of the hand-held flame torch. Subsequently, the far less noisy measurements during the cool-down period are used in the analysis. Furthermore, at the initial phase of cool down, the temperature within the specimen is still not uniform, as it takes ~2–3 s to reach thermal equilibrium across the entire length of the specimen. Thus, the measurements obtained during the first few seconds of cooling (~30 °C drop) are discounted.

In this investigation, YSZ coatings were plasma-sprayed under different conditions onto Al6061 substrates, and subjected to thermal cycling as described above. Fig. 1b shows a typical curvature–temperature plot during cycling from room temperature to 320 °C. The thickness of this coating is 764 μm, while that of the substrate is 3.4 mm. At the onset of heating, the coating is in compression owing to the mismatch in the coefficients of thermal expansion (CTE), and the initial curvature $\kappa_R$ at the room temperature $T_R$ is non-zero. As the specimen is heated during the thermal cycle, the coating stress tends to be tensile, and the curvature shifts its sign as shown in the figure. Here, the zero-curvature is denoted as $\kappa_0$ and the corresponding temperature is denoted as $T_0$. A notable characteristic of these data is the obvious non-linear dependence of curvature with temperature. The curve is steeper at lower temperatures, suggesting a higher stiffness in this region. Since the properties of YSZ are not thermally dependent in this temperature range, the non-linearity is likely to be driven by geometrical/microstructural attributes, and affected by the stress state (i.e., tension vs. compression) of the coatings. Although curvature–temperature behavior is for the most part elastic, some specimens exhibit clearly different paths during heating and cooling phases. This cyclic hysteresis is likely to be caused by crack face sliding and associated friction, and the properties of TS ceramics are more accurately described as 'anelastic'. The investigation of such a phenomenon is beyond the scope of the present work and will be the subject of a future publication. The observed non-linear phenomena and associated relationships presented in this paper are independent of these effects. Here, the effects of various processing conditions on the non-linear elastic behavior of coatings from their curvature–temperature relations are presented, using a novel identification method.

## 3. Identification of non-linear property

### 3.1. Constitutive model

In order to describe the coating's non-linear behavior, a phenomenological constitutive model is introduced. Firstly, based on the experimental observations and likely physical causes of non-linearity (cracks and defects), the stress–strain relation is expected to be asymmetric under tension and compression. Secondly, under very large com-

pression, the response should be nearly linear, as many cracks and thin defects are closed. Thirdly, the transitions from linear to non-linear generally do not occur at the zero stress ($\sigma = 0$). With these factors, the following uniaxial stress–strain model is proposed.

$$\varepsilon = \begin{cases} \frac{\sigma}{E} - \frac{|\sigma_T|^n}{E\sigma_N^{n-1}} & \text{for } \sigma < \sigma_T \\ \frac{\sigma}{E} + \frac{(\sigma-\sigma_T)^n - |\sigma_T|^n}{E\sigma_N^{n-1}} & \text{for } \sigma \geqslant \sigma_T \end{cases} \tag{2}$$

Here, the transitional stress $\sigma_T$ corresponds to the change from linear to non-linear relations, generally negative (i.e., $\sigma_T < 0$). Note that, if $\sigma_T = 0$, the relation simplifies to $\varepsilon = (\sigma/E) + (\sigma^n/E\sigma_N^{n-1})$ under tension, which represents a combination of the linear elastic and modified Ramberg–Osgood models. It is important to note that, owing to the nature of TS coating microstructures, it is expected that there is no clear 'transition' from linear to non-linear regimes, as some cracks continue to close below $\sigma_T$. Also $E$ is Young's modulus, $n$ is the power-law exponent and $\sigma_N$ is a reference stress. A small value of $\sigma_N$ signifies a higher degree of non-linearity, while $\sigma_N \to \infty$ for linear elastic.

A schematic of the stress–strain curve according to Eq. (2) is shown in Fig. 2. Here, the stress–strain axes ($\sigma^* - \varepsilon^*$) centered at $\sigma = \sigma_T$ separate the linear and non-linear regimes. This relation turns out to be very versatile for describing the stress–strain behavior of TS coatings with a minimum number of parameters ($E$, $\sigma_N$, $n$ and $\sigma_T$). Under multi-dimensional conditions (e.g., plate bending), Poisson's ratio $v$ is also required. Also note $E$ is appropriately described as the elastic tangent modulus near room temperature, as it is not the modulus at $\sigma = 0$. A number of measured data were used to examine the suitability of the proposed material model. Other, perhaps more refined, forms of stress–strain relation describing the mechanical
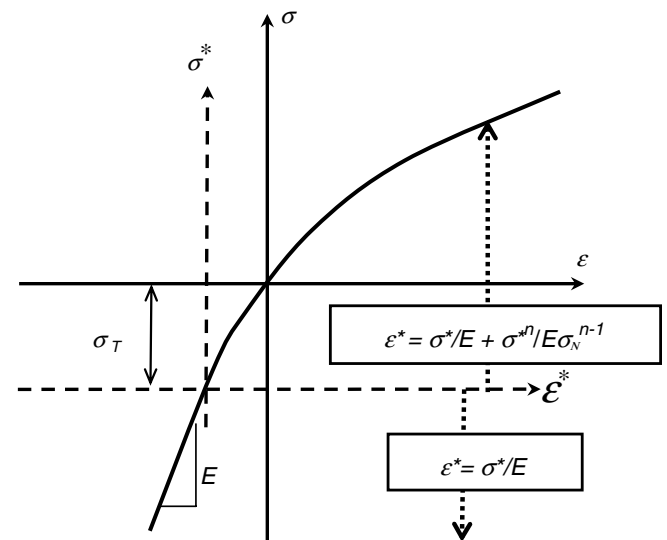


Fig. 2. Non-linear stress–strain relation model for ceramic coatings. Change in stress–strain relation (linear to non-linear) occurs at the transitional stress $\sigma_T$. Here, the $\sigma^*$ and $\varepsilon^*$ axes through this point and the relation with respect to these axes are noted.

behavior of TS coatings are also possible, but they would require more parameters to define the relation.

## 3.2. Non-linear bimaterial beam solution

To extract material parameters of many specimens, a robust procedure, without requiring large-scale computations such as a finite element analysis, is needed. Here, the formulation for a non-linear bimaterial beam solution is described. This procedure is straightforward, yet the derivation is rather complex owing to the shifting of the neutral axis as stress changes (unlike the linear elastic model). Furthermore, although there have been studies on large deformation effects on beams and plates (e.g., Ref. [25]), it was not possible to find solutions for the non-linear elastic bimaterial beams.

Suppose a bimaterial specimen consists of a non-linear elastic coating and linear elastic substrate, as shown in Fig. 3. The axial strain within the coating under temperature change $\Delta T$ is

$$\varepsilon_c(y) = -\Delta\kappa(y - y_0) + \alpha_c\Delta T + \frac{F_{mis}}{bE_c^* t} \tag{3}$$

Here, $\Delta\kappa$ is the curvature change under temperature variation $\Delta T$, $\alpha_c$ is the coefficient of thermal expansion, $y_0$ is the location of the neutral axis, $F_{mis}$ is the mismatch force needed to equilibrate thermal expansions of coating and substrate, $t$ is the coating thickness and $E_c^*$ is the secant modulus, defined as $E_c^* = \sigma_c/\varepsilon_c^m$. Also $\sigma_c$ is the axial stress and $\varepsilon_c^m$ is the mechanical strain (i.e., $\varepsilon_c^m(y) = \varepsilon_c(y) - \varepsilon_c^{therm}$) in the coating. Unlike the linear elastic coatings, the neutral axis shifts with change in the secant modulus as

$$y_0 = \frac{E_s h^2/2 + \int_h^{h+t} E_c^*(y) y \, dy}{E_s h + \int_h^{h+t} E_c^*(y) \, dy} \tag{4}$$

Here, $E_s$ and $h$ are Young's modulus and the thickness of the substrate, respectively. The moment $M_{mis}$ (per thickness) generated by the mismatch force $F_{mis}$ can be shown as

$$\frac{M_{mis}}{b} = \frac{F_{mis}}{b}\left(\frac{h+t}{2}\right) = \frac{E_s E_{ave}^* ht}{E_s h + E_{ave}^* t}\left(\frac{h+t}{2}\right)\Delta\alpha\Delta T \tag{5}$$

In the above, $\Delta\alpha = \alpha_s - \alpha_c$ and $E_{ave}^*$ is introduced as the average secant modulus through the thickness of the coating. The curvature change relates to the moment as $\Delta\kappa = M_{mis}/(EI)_{bimaterial}$. Here, $(EI)_{bimaterial}$ is the effective flexural composite stiffness which varies with the neutral axis and

the secant modulus. With these relations, the curvature change may be expressed as

$$\Delta\kappa = \frac{\frac{E_s E_{ave}^* ht}{E_s h + E_{ave}^* t}\left(\frac{h+t}{2}\right)\Delta\alpha\Delta T}{E_s h\left(\frac{h^2}{3} - hy_0 + y_0^2\right) + \int_h^{h+t} E_c^*(y)(y - y_0)^2 \, dy} \tag{6}$$

Since $y_0$ is not constant during thermal loading, the above formula requires several iterations for a given $\Delta T$. The iteration loops can be reduced by assuming the following form:

$$\Delta\kappa \cong \frac{6 E_s E_{ave}^* ht(h+t)\Delta\alpha\Delta T}{E_s^2 h^4 + E_{ave}^{*2} t^4 + 2 E_s E_{ave}^* ht(2h^2 + 3ht + 2t^2)} \tag{7}$$

In the above, the secant modulus $E_c^*(y)$ in the integral (6) is replaced with the average value $E_{ave}^*$. A similar assumption can be made for the computation of $y_0$ in Eq. (4). To reduce the computational requirement further, instead of computing the correct average value, $E_{ave}^*$ can be estimated at the midpoint of coating ($y = h + t/2$) as

$$E_{ave}^* \cong \frac{\sigma(\varepsilon_c^{mid})}{\varepsilon_c^{mid}} \quad \text{where} \quad \varepsilon_c^{mid}$$

$$= -\Delta\kappa\left(h + \frac{t}{2} - y_0\right) + \frac{E_s h}{E_s h + E_{ave}^* t}\Delta\alpha\Delta T \tag{8}$$

Clearly, the computation of $E_{ave}^*$ still requires multiple iterations. The curvature formula (7) for the non-linear beam appears to be similar to the one given for the linear elastic case (1). However, the required computations are very different, and the determination of unknown material properties for a given $\Delta\kappa - \Delta T$ record is not a simple process. First, the axial strain at the mid-point is initialized as $\varepsilon = \Delta\alpha\Delta T$ (note $\varepsilon = \varepsilon_c^{mid}$). Then the stress is computed via the constitutive Eq. (2) with iterations. Once the average secant modulus and neutral axis are calculated, the curvature can be solved. With this curvature, the strain is updated and the convergence is checked. The iteration is repeated until the required tolerance, generally set as $\Delta\alpha\Delta T/100$, is met.

## 3.3. Inverse analysis to estimate unknown parameters

The constitutive Eq. (2) has four parameters $E_c$, $\sigma_N$, $n$ and $\sigma_T$ to be defined. To estimate them, a multi-step procedure is used. Firstly, the initial tangent modulus $E_c$ near room temperature is determined. Here, the slope of the linear portion of the curvature–temperature curve ($\Delta\kappa/\Delta T$), shown in Fig. 4, and the bimaterial formula for linear elastic materials (Eq. (1)) are used to determine $E_c$. Secondly, the determination of the non-linear parameters is carried out. Here, the process can be simplified by shifting the $T$ and $\kappa$ coordinates as $T^* = T - T_T$ and $\kappa^* = \kappa - \kappa_T$, respectively. The stress and strain are readjusted once the parameters are determined. Thirdly, to obtain the best estimates of $\sigma_N$ and $n$ from the curvature–temperature ($T > T_T$), an inverse analysis is used as described next. Finally, the transitional stress $\sigma_T$ and also the residual stress $\sigma_{RT}$ at room temperature (20 °C) can be obtained.
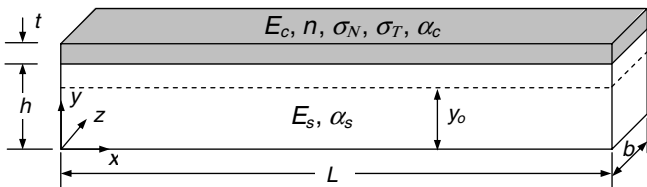


Fig. 3. Schematic of TS coating on substrate with relevant dimensions. Corresponding material parameters are noted, and the location of neutral axis $y_0$ is shown.
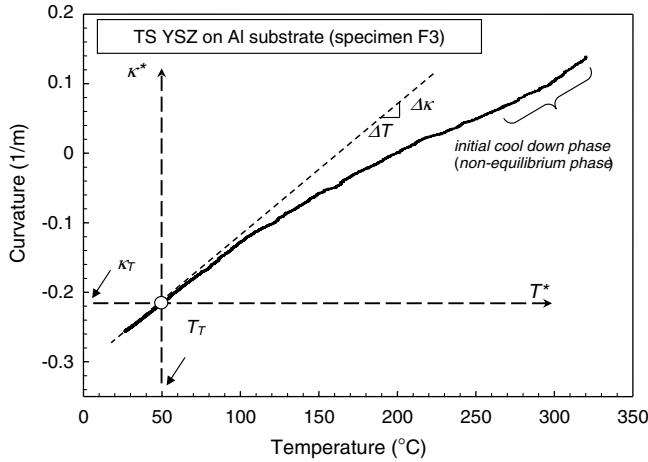
Fig. 4. Identification of transitional point (linear to non-linear) to extract initial tangent modulus $E_c$ from $\Delta T$ and $\Delta\kappa$. Shifted coordinates centered at $T_T$ and $\kappa_T$ are also shown.

The present inverse analysis uses the Kalman filter technique [26–28] to estimate the reference stress $\sigma_N$ and the power-law exponent $n$. Essentially, the algorithm updates the previous estimates based on indirect measurements of unknown state variables and covariance information and attempts to find the best estimate. In the formulation, two unknown parameters are expressed in a state vector form as $\boldsymbol{x}_t = [(\sigma_N)_t, n_t]^T$. Here, $t$ may represent the actual time as well as the temperature (e.g., from $T_{min}$ to $T_{max}$). The procedure is carried out with the following updating equation:

$$\boldsymbol{x}_t = \boldsymbol{x}_{t-1} + \boldsymbol{K}_t[\kappa_t^{meas} - \kappa_t(\boldsymbol{x}_{t-1})] \qquad (9)$$

Here, $\boldsymbol{K}_t$ is the Kalman gain matrix, and $\kappa_t^{meas}$ is the measured curvature at $t$. Also $\kappa_t(\boldsymbol{x}_{t-1})$ is a curvature computed with estimated state parameters at the previous increment. In the above equation, the Kalman gain matrix multiplies the difference between the measured and computed curvature, and it is given as

$$\boldsymbol{K}_t = \boldsymbol{P}_t(\boldsymbol{\kappa}_t')^T \boldsymbol{R}_t^{-1} \qquad (10)$$

where $\boldsymbol{P}_t = \boldsymbol{P}_{t-1} - \boldsymbol{P}_{t-1}(\boldsymbol{\kappa}_t')^T(\boldsymbol{\kappa}_t'\boldsymbol{P}_{t-1}\boldsymbol{\kappa}_t'^T + \boldsymbol{R}_t)^{-1}\boldsymbol{\kappa}_t'\boldsymbol{P}_{t-1}$.

With two state parameters and one measured parameter, the size of the Kalman gain matrix is $2 \times 1$. Also $\boldsymbol{\kappa}_t'$ is a vector that contains the gradients of $\kappa_t$ with respect to each parameter. In addition, $\boldsymbol{P}_t$ is the measurement covariance matrix related to the range of unknown state parameters, and $\boldsymbol{R}_t$ is the error covariance matrix related to the size of measurement error. Once the initial values are imposed, $\boldsymbol{P}_t$ is updated at every step, while $\boldsymbol{R}_t$ is prescribed at each step. In many cases, fixed values can be assigned to $\boldsymbol{R}_t$ as long as measurement error bounds do not vary substantially. As the convergence rate is sensitive to the values of $\boldsymbol{P}_t$ and $\boldsymbol{R}_t$, proper assignments for these two matrices are essential. The initial measurement covariance matrix $\boldsymbol{P}_0$ is set according to the estimated ranges of state parameters (i.e., domain of unknowns), while the constant error

covariance matrix $\boldsymbol{R}_t$ is chosen based on the estimated measurement error for the curvature measurements ($\sim$1% of total curvature change).

In many problems, forward solutions to relate state parameters to measurement parameters and their gradients require computations such as finite element analysis. However, in this case, the established analytical curvature–temperature relation in Section 3.2 can be used to compute the required $\kappa_t$ and $\boldsymbol{\kappa}_t'$. The accuracy of the present procedure was tested with independent numerical simulations in [28].

### 3.4. Sample implementation

As described earlier, the substrate curvature technique was used for the entire investigation, and Al6061 was chosen as the substrate material. There were several reasons for this. Primarily, aluminum provided significant deflection, owing to relatively low stiffness, and high thermal mismatch with YSZ, for high fidelity curvature measurements, which would allow careful extraction of non-linear parameters in thick top coats. Also, YSZ tended to bond well to the aluminum substrate, and the high thermal conductivity of aluminum also reduced the propensity for thermal gradients in the substrate. Similar studies were also conducted with steel-based substrates, but the YSZ bonded poorly to the steel and resulted in delamination. Experiments with superalloy substrates and bond coats (e.g., NiCrAlY) are also under consideration for the three-layer model.

Here, the above proposed procedure is applied to estimate the unknown properties of an actual TS ceramic coating. The cooling phase of the curvature–temperature curve is used to estimate $E_c$, $\sigma_N$, $n$ and $\sigma_T$. For this and all other specimens, the properties of the Al6061 substrate are assumed to be temperature dependent [29] following:

$$\begin{aligned} E_s(T) &= -2.65 \times 10^{-7}T^3 + 2.4 \times 10^{-4}T^2 - 9.21 \times 10^{-2}T \\ &\quad + 85.2 \text{ (GPa)} \quad \text{for } 113 \text{ K} < T \leqslant 573 \text{ K} \\ \alpha_s(T) &= -9.27 \times 10^{-12}T^2 + 2.59 \times 10^{-8}T \\ &\quad + 1.54 \times 10^{-5} \text{ (1/K)} \quad \text{for } 283 \text{ K} < T \leqslant 575 \text{ K} \end{aligned}$$
$$(11)$$

Note that the inclusion of the above temperature-dependent properties for aluminum is critical in terms of estimating accurate properties for TS coatings.

From the results shown in Fig. 4, the transitional temperature is identified as $T_T = 50 \,^\circ\text{C}$. The corresponding transitional curvature is $\kappa_T = -0.22 \text{ m}^{-1}$. As the curvature change is gradual, precise determination of the transitional point is often difficult. In order to quantify the effects of variation in $T_T$, the properties for $T_T = 30$ and $60 \,^\circ\text{C}$ were also estimated. The differences in the modulus were within $\pm 1.7\%$ and the variations in stress–strain relations were well within the error bounds. Thus, a slight variation in $T_T$ appears to have limited influence on the resulting estimated stress–strain curves.

Next, two non-linear parameters, $\sigma_N$ and $n$, are estimated with the Kalman filter procedure. Here, in order to facilitate the interpretation, initially a simpler form of constitutive equation was used, with $\sigma_T = 0$ in Eq. (2). Once the non-linear parameters are estimated, $\sigma_T$ is computed from the difference between zero and the transitional curvature values. As described earlier, owing to the non-equilibrium thermal state, the data from initial cool down phase were not used during the estimation of the properties. Here, 30 data points within $50\,°C < T < 274\,°C$ are selected for the inputs in the Kalman filter. The initial estimates of $\sigma_N$ and $n$ are chosen as follows: Within the domain of $10\,MPa < \sigma_N < 90\,MPa$ and $1 < n < 4$, $\sigma_N$ and $n$ are incremented into 40 intervals to generate $41 \times 41 = 1681$ sets of initial estimates. Each set of initial estimates is processed through the Kalman filter, and the final estimates are obtained after 30 steps. In general, different initial estimates do not merge at the same point but a robust procedure should generate a small domain of convergence. The best estimates can then be made from the weighted average of converged values. The estimates are $\sigma_N = 37\,MPa$ and $n = 3.2$, respectively. Afterwards, the transitional stress and the residual stress are computed as $\sigma_T = -32\,MPa$ and $\sigma_{RT} = -38\,MPa$, respectively. The error bounds are estimated as $\Delta E_C = \pm 2\,GPa$, $\Delta\sigma_N = \pm 3\,MPa$ and $\Delta n = \pm 0.2$, based on the repeatability of measurements and the sensitivity of solutions. It is also noted that, as different combinations of $\sigma_N$ and $n$ yield the same strain according to the uniaxial model (2), very precise determinations of $\sigma_N$ and $n$ are difficult, especially from the single measurement of curvature. However, the estimated stress–strain curves from different combinations of $\sigma_N$ and $n$ would still look very similar, as well as the results of any post analyses using such curves.

Using these parameters, the stress–strain relation is reconstructed, as shown in Fig. 5. The two circles represent the bounds at room temperature ($20\,°C$) and maximum
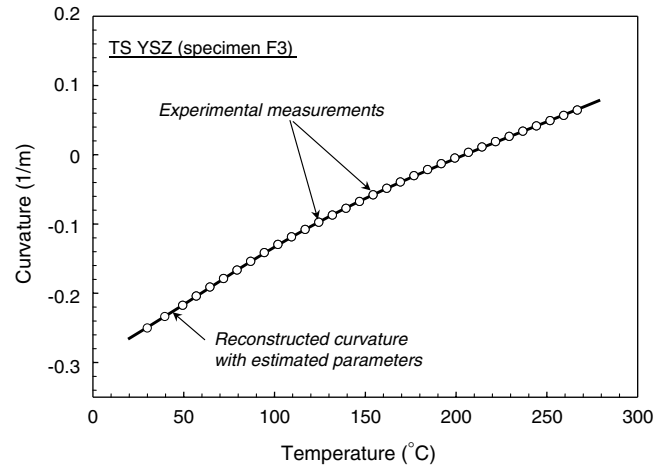


Fig. 6. Comparison between measured (circles) and simulated (solid line) curvature. The latter is calculated by assigning the best estimates as properties in the non-linear bimaterial formula.

temperature ($274\,°C$). Essentially, the slopes outside these bounds are extrapolated results, as only the records between these temperatures are actually used to estimate the property. Note that the coating may behave in a different way outside the range, especially under large tensile load (e.g., further cracking).

In most inverse analyses, there is no independent way to prove that best estimates are indeed correct or near-correct solutions. However, there are two ways to judge the accuracy. One is based on the convergence behavior of various initial estimates. A small domain of convergence implies the robustness of the inverse method, as many initial estimates converged near the same location (i.e., similar estimates). The present analysis generated small domains of convergence, and thus support the accuracy of the estimates. Additional confirmation can be made from re-creation of the curvature–temperature plot. Using the best estimates as inputs, the curvature–temperature relation was re-computed using the non-linear bimaterial formula, as shown in Fig. 6. Its agreement with the measured curvature is excellent, as the measured data (shown with circles) essentially lie on top of the reconstructed curve with the estimated parameters. Thus, for the present material model, the estimated parameters represent accurate measures of the coating properties.

## 4. Effects of processing parameters on coating properties

The above non-linear analysis method was used to investigate effects of various process conditions on the non-linear mechanical properties of TS YSZ coatings. Here, the effects of the following processing conditions are discussed:

- variations in feedstock size distributions, which affect not only the particle state but the splat morphology and deposit characteristics as well;
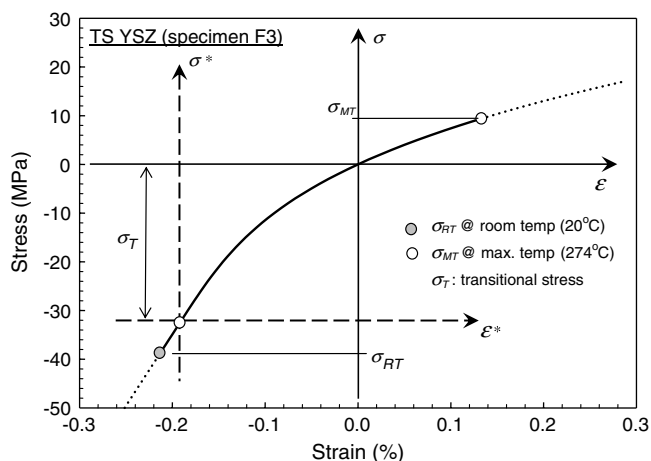


Fig. 5. Non-linear stress–strain relation computed with best estimates. The shifted coordinates whose origin is at the transition point are also shown.

- different feedstock morphologies with known implications in thermo-mechanical performance of TBCs [30];
- variations in in-flight particle temperature and velocity as affected by torch conditions;
- other deposition conditions of critical importance for actual components, including spray distance and angle.

Over 50 experiments were conducted through the course of this investigation but, for the sake of brevity, only selected results from the above are presented here. The tabulated processing conditions for different specimens are listed in Table 1.

### 4.1. Effect of feedstock particle size distribution

Feedstock particle size is one of the key parameters that affect the deposit microstructure. Particle size affects the molten fraction of particles during plasma spraying. In particular for YSZ, smaller particles are desired, given the high melting temperature and low thermal conductivity of the particles. However, other important attributes influence deposit formation. For instance, smaller particle size yields thinner splats (due to better melting) and more compaction (due to higher velocities), resulting in greater deposit den-

sity and a smoother surface. However, smaller particle size will also result in a larger fraction of splat interfaces per unit thickness of the coating. Several previous studies have investigated the effects of starting particle size on the melting, deposit formation dynamics, microstructure and properties of the coatings [3,10,31]. Significantly higher modulus (obtained via indentation) and hardness were observed for the coating produced using fine powder, with a smoother surface and fewer unmelted particles.

For this investigation, a single powder morphology, fused and crushed (FC), was chosen with three different size distribution referred to as fine, coarse and ensemble, with 10–45 μm, 45–75 μm and 10–75 μm powder sizes. They were sprayed by air plasma on an aluminum (Al6061) substrate under similar controlled processing parameters, including spray distance, final coating thickness and spray angle, as listed in Table 1.

Curvature–temperature records (Fig. 7a) were used to characterize the coating properties through the procedure described in Section 3. Continuous stress–strain relations of the coating in the experimental temperature range from room to maximum temperatures were identified, as shown in Fig. 7b. The estimated parameters are listed in Table 1. The results confirm that the in-plane modulus at room

Table 1
Processing conditions and estimated properties of various TS YSZ coatings

| | Processing conditions | | | | | | Estimated properties | | | | |
|---|---|---|---|---|---|---|---|---|---|---|---|
| | Size | Powder | Particle T (°C) | Particle V (m s⁻¹) | Other conditions | Thickness (μm) | $E_c$ (GPa) (±2 GPa) | $\sigma_N$ (MPa) (±3 MPa) | $n$ (±0.2) | $\sigma_T$ (MPa) (±3MPa) | $\sigma_{RT}$ (MPa) (±3 MPa) |
| Effects of powder size | | | | | | | | | | | |
| P1 | Fine | FC | 2617 | 113 | NA | 433 | 30 | 37 | 1.7 | −29 | −37 |
| P2 | Coarse | FC | 2587 | 101 | NA | 424 | 22 | 34 | 1.9 | −27 | −33 |
| P3 | Ensemble | FC | 2547 | 95 | NA | 414 | 23 | 43 | 2.2 | −27 | −33 |
| Effects of powder morphology/feedstock | | | | | | | | | | | |
| F1 | Ensemble | FC | 2659 | 128 | NA | 696 | 37 | 54 | 2.2 | −38 | −46 |
| F2 | Ensemble | AS | 2661 | 127 | NA | 746 | 34 | 52 | 2.9 | −43 | −51 |
| F3 | Ensemble | HOSP | 2650 | 127 | NA | 764 | 29 | 37 | 3.2 | −32 | −38 |
| Effects of particle temperature and velocity | | | | | | | | | | | |
| V1 | Ensemble | FC | 2504 | 80 | NA | 434 | 22 | 32 | 2.2 | −17 | −18 |
| V2 | Ensemble | FC | 2631 | 103 | NA | 815 | 47 | 45 | 3.1 | −39 | −40 |
| V3 | Ensemble | FC | 2677 | 150 | NA | 615 | 51 | 85 | 2.4 | −53 | −60 |
| Effect of spray distance | | | | Distance (mm) | | | | | | | |
| P3(D1) | Ensemble | FC | 2547 | 95 | 130 | 414 | 23 | 43 | 2.2 | −27 | −33 |
| D2 | Ensemble | FC | 2642 | 107 | 110 | 403 | 28 | 45 | 2.1 | −34 | −39 |
| Effect of spray angle | | | | Angle (°) | | | | | | | |
| A1 | Ensemble | FC | 2547 | 95 | 90 | 776 | 25 | 50 | 1.9 | −23 | −28 |
| A2 | Ensemble | FC | 2515 | 86 | 60 | 660 | 23 | 55 | 3.9 | −26 | −29 |
| Effect of spray speed | | | | Speed (mm s⁻¹) | | | | | | | |
| S1 | Ensemble | FC | 2568 | 100 | 450 | 348 | 23 | 36 | 2.0 | −24 | −30 |
| S2 | Ensemble | FC | 2564 | 99 | 150 | 373 | 25 | 47 | 2.4 | −25 | −30 |
| Effect of coating thickness | | | | | | | | | | | |
| T1 | Coarse | FC | 2576 | 102 | NA | 960 | 27 | 50 | 1.8 | −25 | −30 |
| P2(T2) | Coarse | FC | 2587 | 101 | NA | 424 | 22 | 34 | 1.9 | −27 | −33 |

P3 and D1, P2 and T2 are identical. Unless noted: feed rate = 30 g/min, spray distance =130 mm, angle = 90°, speed = 300 mm s⁻¹.
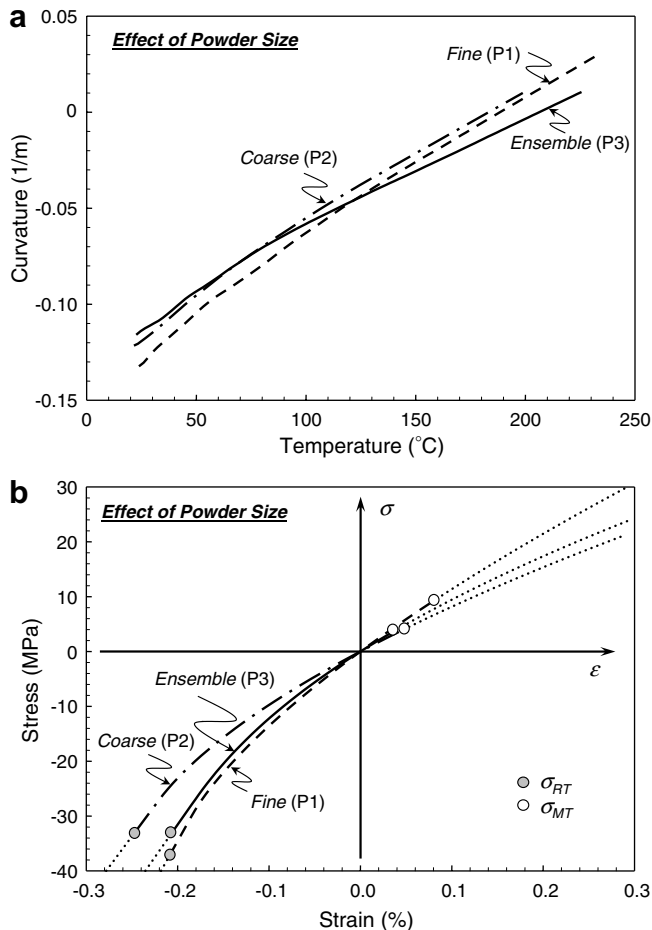
Fig. 7. Effect of different FC feedstock size processed under similar conditions, fine (dia. ∼10–45 μm), coarse (∼45–75μm) and ensemble (∼10–75μm): (a) measured substrate curvatures; (b) estimated stress–strain relations.

temperature increases as powder size decreases, resulting from improved coating density (this was confirmed from other density and porosity measurements as well). All three coatings show non-linear stress–strain behavior while, not surprisingly, a stiffer mechanical response is observed for coating produced by fine powder. As the coatings have many microcracks and pores, the opening cracks give rise to the more compliant response of coating with increasing tension. Once the cracks close or partly close, coatings show a stiffer response. It is interesting to observe that, in the ensemble curve, powder with large variation in particle sizes (i.e., equal mixture of fine and coarse grains) falls between the other two.

As described for Fig. 5, bounds of stress change during thermal cycle are indicated as circles in Fig. 7b. Although it is likely that the stress–strain relation would follow the extrapolated path at least to some extent, specimens were not subjected outside these bounds. Note that, for these specimen, the stresses at corresponding maximum temperatures ($T_{max} = 200$–230 °C) reach a very low tensile state. However, the amplitudes of residual stresses at room tem-

perature are significant, reaching −37 MPa for fine powder and −33 MPa for both coarse and ensemble powder.

### 4.2. Effect of powder morphology/type of feedstock

In the case of YSZ, starting feedstock morphology can strongly affect the microstructure of the coating [30]. This is because the nature of flame–particle interactions with respect to the behavior of the particles in-flight significantly contributes to microstructural variations. Here, three morphologies commonly used for YSZ coatings are briefly described: fused and crushed (FC), agglomerated and sintered (AS) and plasma densified hollow sphere (HOSP). FC powders are very dense, with the angular/polyhedral morphology, AS powders are globular, and HOSP powders are hollow spheroids [30–32]. In this study, comparable size distributions of all three morphologies of feedstock mentioned above were used.

In an effort to normalize potential variance in particle state, the process parameters were optimized such that the averages and distributions in particle temperatures and velocities (averaged >10,000 particles) for each of the morphologies were kept nominally constant. In fact, even the distributions of temperature and velocity were kept relatively similar by relatively close choice of process parameters. The procedure used to accomplish such optimization through process control is a significant study in itself and is partially described in [33].

From the curvature measurements shown in Fig. 8a and the present identification procedure, mechanical properties were determined as listed in Table 1. Coating sprayed with FC powders shows a higher modulus compared with those sprayed with the HOSP and AS powders. The stress–strain relations in Fig. 8b show their non-linear behavior. The HOSP material displays a larger compliance in tension and a higher degree of non-linearity compared with the other morphologies. In fact, it has been anecdotally reported in industrial work that the HOSP material has had beneficial thermo-mechanical response in service. The origin of such a response is related to the larger fraction of interfaces created during consolidation of the hollow powder (lower density). Although establishment of a detailed microstructure–non-linearity relation requires further investigation, some connections are described in Section 5.

### 4.3. Effect of particle temperature and velocity

Particle temperature and velocity are known to have a strong influence on the melting and flattening of particles, affecting droplet solidification and adhesion among the splats. Temperature and velocity are two of the most important parameters influencing the coating microstructure. Friis et al. [8] showed that an increase in temperature and velocity of particles results in a decrease in total porosity and denser coatings. Particles of high temperature and velocity possess high kinetic energy and low viscosity,
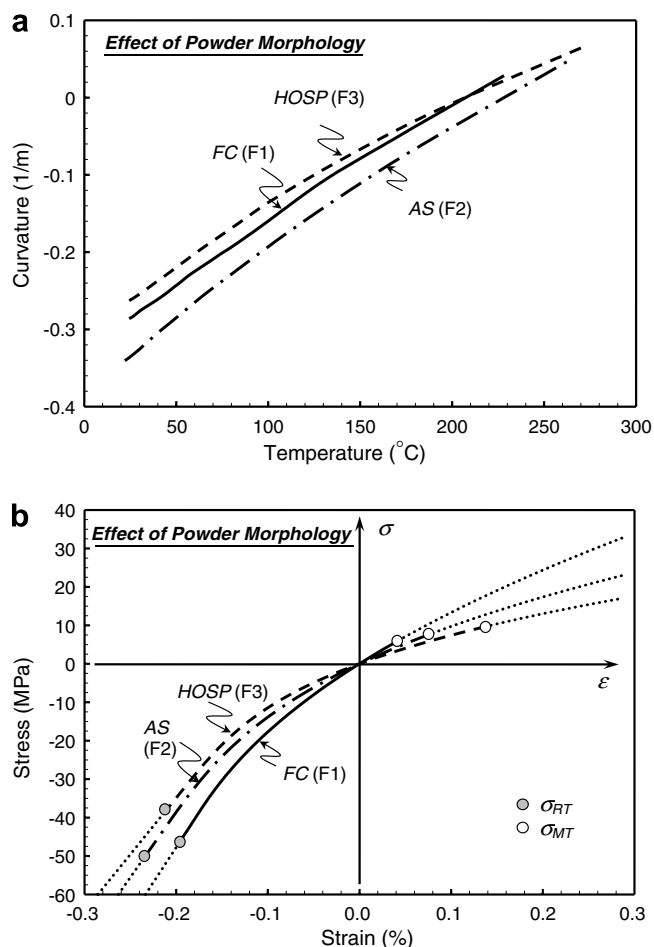
Fig. 8. Effect of different feedstock morphology processed under similar conditions for FC, AS and HOSP: (a) measured substrate curvatures; (b) estimated stress–strain relations.
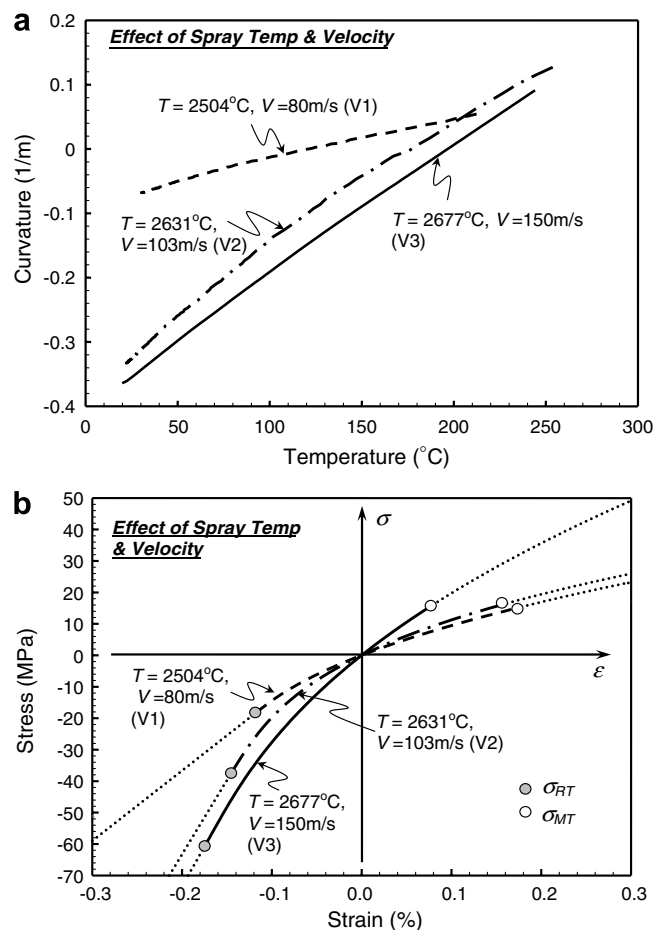


Fig. 9. Effect of different particle temperatures and particle velocities: (a) measured substrate curvatures; (b) estimated non-linear stress–strain relations.

which lead to the particles' better filling the irregularities in the deposited splats.

To investigate the dependence of the non-linear response of the YSZ coating with the particle state, an operational parameters space was explored. First, a design of experiments approach was used to investigate the particle temperature velocity space for the particular powder and spray conditions. Subsequently, three conditions with differences in particle temperatures and velocities were identified, and coatings were fabricated. The three resultant coatings were made from particle streams with average temperatures and velocities (in increasing order) of 2504 °C, 80 m s$^{-1}$, 2631 °C, 103 m s$^{-1}$ and 2677 °C, 150 m s$^{-1}$, respectively. Fig. 9 presents the curvature–temperature relationships for the three above coatings and the corresponding non-linear stress–strain relations. One can clearly see that the coatings produced at low particle temperature and velocities have a greater compliance compared with the higher temperature and velocity sample. These results quantitatively and robustly confirm the conventional 'rule of thumb' from the point of view of process–microstructure correlation. Note that, although the

thicknesses of three specimens are not similar here, the effects of particle temperature and velocity appear much greater than the thickness effect described below.

### 4.4. Effects of other parameters

Figs. 10 and 11 show additional examples of parametric effects, including spray distance, angle, speed and coating thickness. All these other parameters are important to industry, as the turbine is a complex 3D object, and there are spatial microstructural distinctions within the coating, depending on geometry and associated changes in spray distance, torch speed and deposition angle.

The results indicate that the coating was somewhat more non-linear when it was sprayed from a greater distance (from 130 mm). Spraying at an angle (at 60°) produces a much more non-linear specimen. Although it is not apparent from Fig. 10b, while $\sigma_N$ values are similar for both cases, $n$ values are 1.9 for the 90° specimen and 3.9 for the 60° specimen. The spray speed affects the number of particles per unit area per unit time and can modify the evolution of the microstructure. The results indicate that the compliance is affected by this parameter. Coating
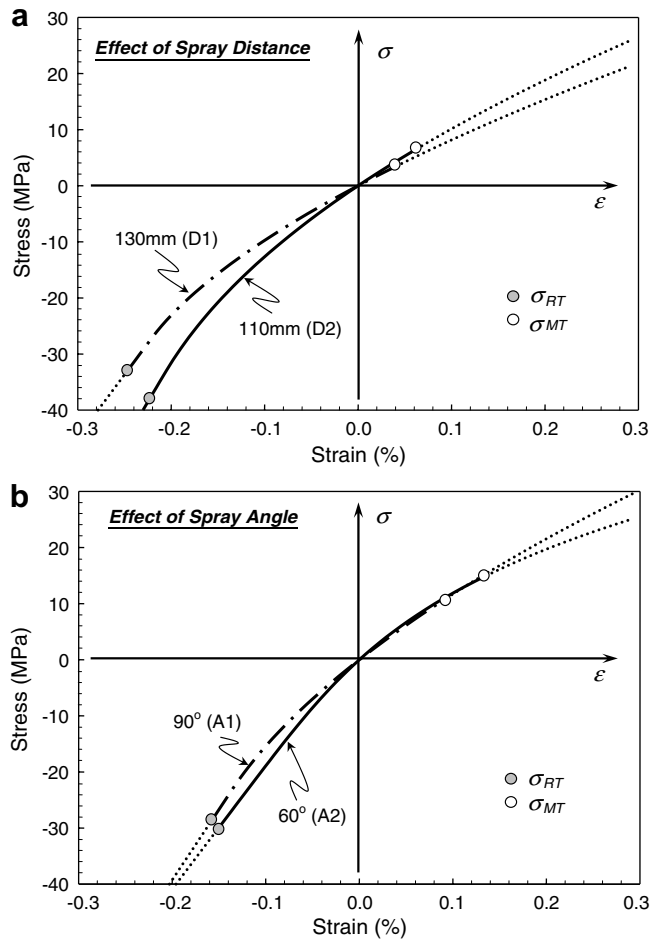
Fig. 10. Estimated non-linear stress–strain relations with different process conditions: (a) spray distance; (b) spray angle.



Fig. 11. Estimated non-linear stress–strain relations with different process conditions: (a) spray speed; (b) coating thickness.

fabricated with a spray speed of 150 mm s$^{-1}$ is more densified and stiffer than that fabricated with a spray speed of 450 mm s$^{-1}$.

The influencing parameters are not limited to powder and spray conditions. The deposited coatings posses different mechanical characteristics if they have different final thicknesses. Two specimens with different thicknesses, shown in Fig. 11b, exhibit very different stress–strain relations. In fact, the thinner coating ($t = 424$ μm) is more compliant and non-linear than the thicker one ($t = 960$ μm). (In exploring the various process variations, the thicknesses of the various coatings were kept relatively similar to avoid this effect.) It is possible that different heat transfer conditions after deposition produce dissimilar microstructures during the cool-down period. These examples further demonstrate the utility of the proposed approach in quantifying the mechanical attributes of these non-linear ceramic coatings.

### 4.5. Summary of results

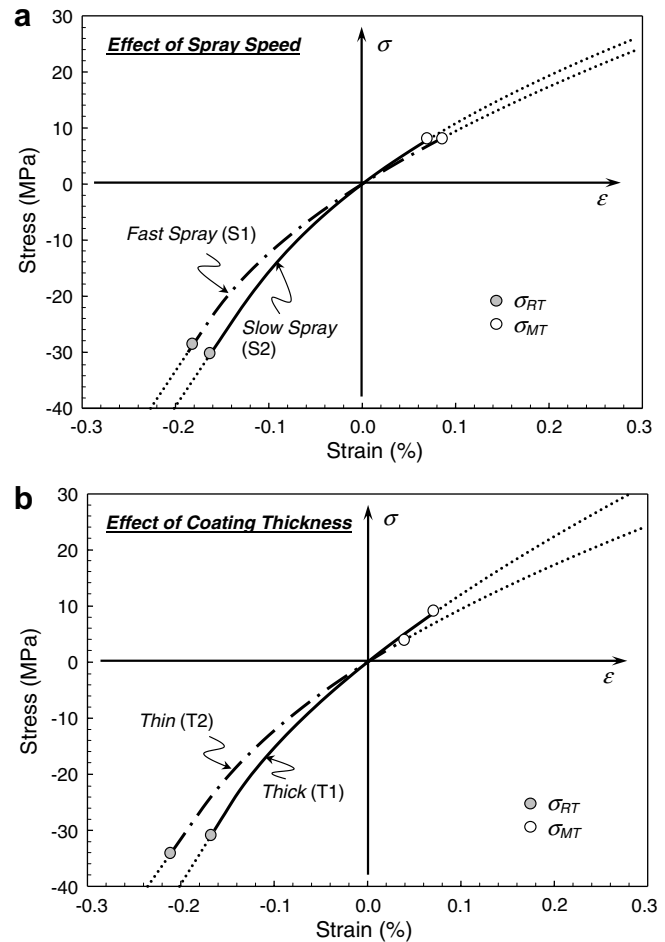It can be argued that a coating is likely to exhibit higher non-linearity when it possesses a high density of embedded micro-cracks, as opening and closing of these cracks cause such behavior. The initial results suggest that non-linearity increases in thinner coatings, coatings sprayed at a tilted angle and those obtained in conditions such as high particle temperature. Rigorous confirmation of these predicted relations between the process conditions and microstructures requires further studies.

The characteristics of each coating's mechanical behavior can be summarized graphically, as shown in Fig. 12. Here, 'non-linear degree' (ND) is introduced to denote the extent of non-linearity as

$$\mathrm{ND} = E/E_{0.001}^*. \tag{12}$$

Here $E$ is the room temperature elastic modulus defined in Eq. (2) and $E_*^{0.001}$ is the secant modulus between the transitional point ($\sigma_T$, $\sigma_T$) and the stress and strain at $\varepsilon = 0.001$. With this definition, a large ND value signifies greater non-linearity while ND = 1 if a coating is linear elastic. The parameter essentially represents the departure of stress-strain relation from its initial linear slope. Note that this form has direct physical significance (i.e., operationally defined), and other formulations are also possible as examined. However this form has shown to be effective in
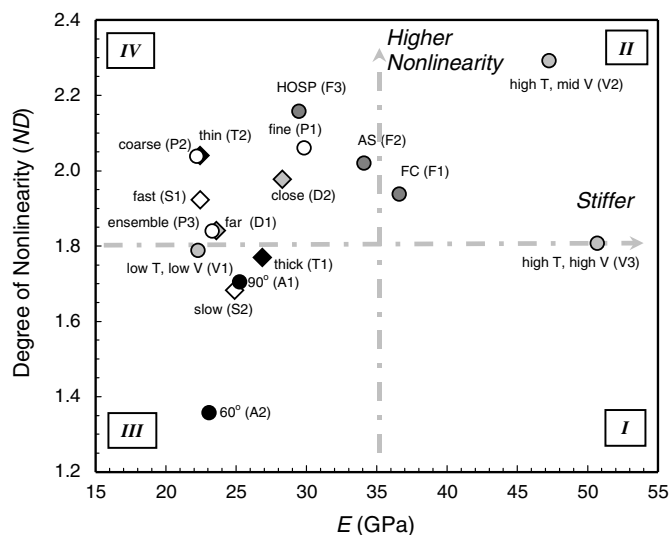
Fig. 12. Graphical representations of non-linear properties of TS YSZ coatings. Quadrangles symbolize: I, stiff throughout loading; II, stiff under compression but compliant under large tension; III, compliant under compression with increasing compliant under tension; IV, compliant throughout loading.

terms of its insensitivity to measurement and interpretation errors. In Fig. 12, this parameter is plotted as a function of the room temperature modulus $E$ for each specimen. In the figure, approximated quadrangles are drawn to classify stress-strain relations of various coatings. Essentially, if a coating falls within the quadrangle I, it is expected to remain stiff throughout the loading. On the other hand, if a coating falls in the quadrangle II, then it tends to more compliant under large tension. Similarly, if a coating stays in the quadrangle III, it is compliant and also expected to be more so under larger tensile load. Lastly if a coating in the quadrangle IV, then its stiffness remains at similar low level regardless of the loading magnitude.

Some observations can be made from this figure. For instance, the coating sprayed under high temperature at mid-velocity (V2) to be initially stiff but tends to be compliant at higher stress. For HOSP powder coating (F3), it is compliant at low stresses and more so under larger stresses. Such a phenomenon is consistent with the high density of interfacial cracks observed in HOSP coating. On the other extreme, a coating fabricated with high temperature and high velocity particles (V3) remains stiff at wide range of stresses (or thermal strain). The figure also suggests the titled spray coating (A2) to be very compliant and stays linear even at higher stresses. These integrated connections between process science and mechanics will enable opportunities for microstructural control for optimal design and performance of thermo-mechanical coatings.

## 5. Discussion

A novel method based on inverse analysis and curvature measurement is presented to estimate the non-linear mechanical property of thermal-sprayed YSZ coating. This technique is attractive, as it does not require complex set-up or lengthy data interpretation. More importantly, it is now possible to make correct interpretations of measured curvature–temperature records. Previously, the non-linear record made even the extraction of the linear elastic modulus uncertain.

The estimated stress–strain relations presented here are qualitatively consistent with those measured under mechanical load [14–16]. Coatings exhibit stiffness response under compression and more compliant response under tension. Although it requires knowledge of CTE, an advantage of curvature measurement under temperature change is that it produces a more uniform stress state within a coating than that under mechanical load, as it does not generate stress concentration near load-points.

In this study, the procedure was used to quantity the effects of both starting YSZ powder particle characteristics and processing parameters on the effective properties. Compared with the linear elastic properties assumed in traditional models, the non-linear stress–strain relations offer a more accurate description of coating behavior. In earlier studies, relationships between the microstructural changes with different spray conditions to curvature/stress–stain
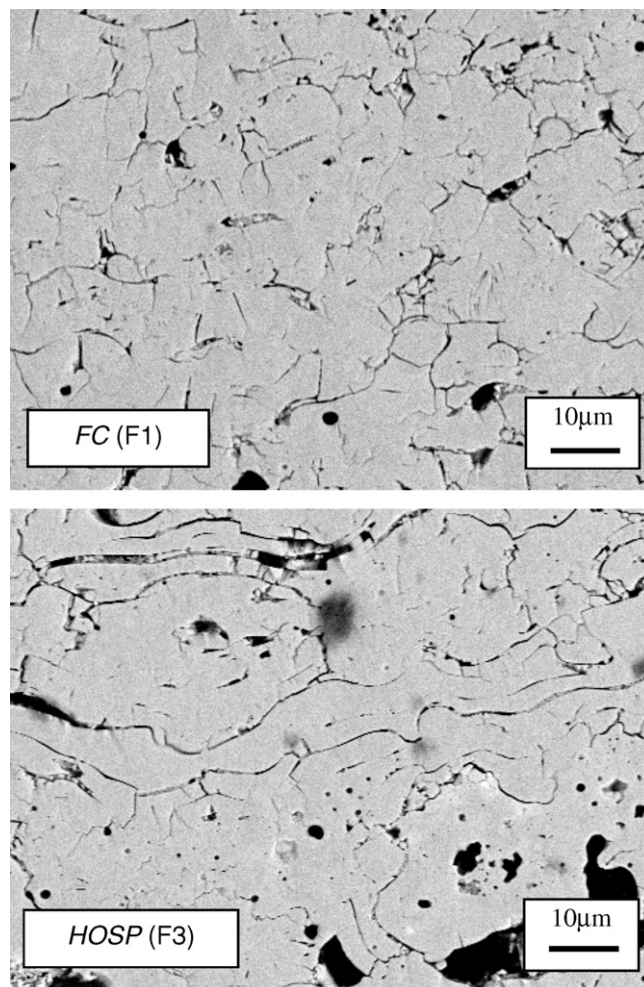




Fig. 13. SEM images of two specimens, FC and HOSP, used to study the effect of feedstock morphology.

were investigated for linear properties [3,8,30–32]. These studies were expansive and comprehensive and examined the microstructure–thermal conductivity and elastic properties for various feedstock and process conditions. The non-linear response closely follows the links between microstructure and properties, as described in the earlier papers. For instance, the SEM images in Fig. 13 show distinctly different morphology of TS coatings with two types of feedstock. The FC coating contains shorter embedded cracks and smaller density of cracks (i.e., total crack lengths per area). However, the HOSP coating contains many long interlamellar cracks and higher crack density. The larger non-linearity observed for HOSP coating (from Figs. 8(b) and 12) is likely to be the result of these cracks, as more of them open and close under tension and compression. Though not obvious here, higher magnification images reveal HOSP also to possess many (partially) closed intra-splat cracks. These observations are consistent with measurements by the small-angle neutron scattering (SANS) technique [30]. They reveal the crack density of HOSP to be ∼50% higher than that of FC, and a higher interlamellar porosity with HOSP as well.

The present tool is particularly interesting in that not only does it quantitatively confirm arguments about coating behavior based on microstructural observations, but it also provides a robust 'check' for new process and/or material feedstock strategies. Further, the relative simplicity of the technique allows its ready use in many spray facilities, elevating the precision with which coating manufacturers may describe and compare their products. Extensions of the current methodology to thermal cycle at higher temperatures and coatings with different substrate materials are also under way.

## Acknowledgements

## References

[1] Ning X, Li C, Li C, Yang G. Vacuum 2006:1261.
[2] Brinkiene K, Kezelis R. J Eur Ceram Soc 2004;24:1095.
[3] Deshpande S, Kulkarni A, Sampath S, Herman H. Surf Coat Technol 2004;187:6.
[4] Zhao L, Maurer M, Fischer F, Dicks R, Lugscheider E. Wear 2004;257:41.
[5] Kadolkar P, Dahotre N. Mater Sci Eng A 2003;342:183.
[6] Li M, Christofides P. Chem Eng Sci 2003;58:849.
[7] Thangamani N, Chinnakali K, Gnanam F. Ceram Int 2002;28:355.
[8] Friis M, Persson C, Wigren J. Surf Coat Technol 2001;141:115.
[9] Mawdsley J, Su Y, Faber K, Bernecki T. Mater Sci Eng A 2001;308:189.
[10] Kweh SWK, Khor KA, Cheang P. Biomaterials 2000;21:1223.
[11] Teixeira V, Andritschky M, Fischer W, Buchkremer HP, Stover D. Surf Coat Technol 1999;120–121:103.
[12] Kroupa F, Plesek J. Mater Sci Eng A 2002;328:1.
[13] Kroupa F, Dubsky J. Scripta Mater 1999;40:1249.
[14] Harok V, Neufuss K. J Therm Spray Technol 2001;10:126.
[15] Eldridge JI, Morscher GN, Choi SR. Ceram Eng Sci Proc 2002;23:371.
[16] Wakui T, Malzbender J, Steinbrech RW. J Therm Spray Technol 2004;13:390.
[17] Menzel S, Strehle S, Wendrock H, Wetzig K. Appl Surf Sci 2005;252:211.
[18] Hunsche B, Vergöhl M, Neuhäuser H, Klose F, Szyszka B, Matthée T. Thin Solid Films 2001;392:184.
[19] Carlotti G, Doucet L, Dupeux M. Thin Solid Films 1997;296:102.
[20] Lacquaniti V, Monticone E, Picotto GB. Surf Sci 1997;377–379:1042.
[21] Krulevitch P, Ramsey PB, Makowiecki DM, Lee AP, Northrup MA, Johnson GC. Thin Solid Films 1996;274:101.
[22] Stoney G. Proc Roy Soc Lond A 1909;82:172.
[23] Tsui YC, Clyne TW. Thin Solid Films 1997;306:23.
[24] Matejicek J, Sampath S. Acta Mater 2003;51:863.
[25] Finot M, Suresh S. J Mech Phys Solids 1996;44:683.
[26] Kalman R. ASME J Basic Eng. 1960;82D:35.
[27] Nakamura T, Wang T, Sampath S. Acta Mater 2000;48:4293.
[28] Nakamura T, Liu Y. Int J Solids Struct 2007;44:1990.
[29] Material Properties Database, JAHM Software Inc.; 1999.
[30] Kulkarni A, Wang Z, Nakamura T, Sampath S, Goland A, Herman H, et al. Acta Mater 2003;51:2457.
[31] Kulkarni A, Vaidya A, Goland A, Sampath S, Herman H. Mater Sci Eng A 2003;359:100.
[32] Wang Z, Kulkarni A, Deshpande S, Nakamura T, Herman H. Acta Mater 2003;51:5319.
[33] Streibl T, Vaidya A, Friis M, Srinivasan V, Sampath S. Plasma Chem Plasma Process 2006;26:73.